Available online at www.sciencedirect.com

ScienceDirect

Ceramics International 40 (2014) 2835–2846

CERAMICS INTERNATIONAL

www.elsevier.com/locate/ceramint

Synthesis, structural and morphological characteristics, magnetic and optical properties of Co doped ZnO nanoparticles

Amalia Mesaros[a], Cristina D. Ghitulica[b], Mihaela Popa[a], Raluca Mereu[a], Adriana Popa[c], Traian Petrisor Jr.[a], Mihai Gabor[a], Adrian Ionut Cadis[d], Bogdan S. Vasile[b,*]

[a]*Technical University of Cluj-Napoca, 28 Memorandumului Street, 400114 Cluj-Napoca, Romania*

[b]*University "Politehnica" from Bucharest, Faculty of Applied Chemistry and Material Science, Department of Science and Engineering of Oxide Materials and Nanomaterials, 1-7, Gh. Polizu Street, 011061 Bucharest, Romania*

[c]*National Institute for Research and Development of Isotopic and Molecular Technologies, 65-103 Donath Street, 400293 Cluj-Napoca, Romania*

[d]*Raluca Ripan Institute for Research in Chemistry, Babes-Bolyai University, Fantanele 30, 400294 Cluj-Napoca, Romania*

Received 23 September 2013; received in revised form 2 October 2013; accepted 9 October 2013
Available online 17 October 2013

Abstract

$Zn_{1-x}Co_xO$ (x==0.05, 0.10, 0.15) nanoparticles have been synthesized by an alternative wet-chemical synthesis route using the SimAdd technique. The as-obtained powders were investigated by FT-IR spectroscopy, X-ray diffraction and thermal analysis correlated with evolved gas analysis (TG–DTA–FT-IR) in order to determine their chemical nature, crystalline structure and to establish the decomposition sequences. The precipitates are generally amorphous, but low-intensity reflection peaks assigned both to the zinc oxalate dihydrate, and zinc hydroxide can be observed in the recorded patterns, indicating that hydroxy-oxalate precipitates were obtained. The structure, morphology and magnetic properties of the thermally treated samples have been investigated by X-ray diffraction, FT-IR, HRTEM, SAED, UV–vis and EPR. XRD studies reveal a hexagonal wurtzite-type structure for all $Zn_{1-x}Co_xO$ samples. TEM investigations show particle size between 28 and 37 nm, with spherical and polyhedral shapes and with tendency to form aggregates. The presence of a Co_3O_4 secondary phase was evidenced by XRD, UV–vis and EPR for the $Zn_{0.85}Co_{0.15}O$ sample. The ferromagnetic behavior of the samples was revealed. The paper highlights that by varying the cobalt concentration it is possible to modulate the structural, morphological, optical and magnetic properties.

Keywords: Co doped zinc oxide nanoparticles; Zinc oxalate; Wet chemical method; TG–DTA–FTIR; TEM–HRTEM

1. Introduction

The scientific research interest in wide band gap semiconductors has been attracted by the zinc oxide (ZnO) due to its excellent properties as semiconducting material [1–7]. ZnO is a II–VI n-type semiconductor with a wide direct band-gap in the near-UV spectral region, at room temperature [8–13] and, a large free-exciton binding energy of 60 meV [7,11–13]. Zinc oxide nanoparticles exhibit a considerable potential for applications in the solar cells field [14–19], diluted magnetic semiconductors [19,20], nanopiezotronics [21,22], UV detectors [23,24], chemical sensors, gas sensors [25], light-emitting diodes and lasers [26,27]. Therefore, the optical properties of ZnO and the possibility of band gap engineering through transitional metal (TM) doping, strongly encourages the exploration of the magneto-optical properties of the ZnO:TM [19,25].

Various chemical and electrochemical synthesis methods have been used to obtain nanostructured Co doped ZnO nanoparticles, such as sol-gel [28,25], precipitation/coprecipitation [29–33], hydrothermal [34,35], microemulsion [36,37], pyrosol [38,39], and electrochemical methods [40,41]. The precipitation/coprecipitation method, as compared with other chemical or physical methods, is an inexpensive method which allows the synthesis of a wide range of nanoparticles with different and controlled sizes and shapes [16,29,30,42,43]. Compared with the classical method of synthesis based on

*Corresponding author. Tel./fax: +40 21 310 7633.
E-mail address: bogdan.vasile@upb.ro (B.S. Vasile).

0272-8842/$ - see front matter
http://dx.doi.org/10.1016/j.ceramint.2013.10.030

solid phase reactions, this method has the advantage that it allows the control of the particle nucleation and growth from the precursor solution. Among these strategies, the precipitation method via oxalate intermediates has been approached in this study. The paper presents a simple, reproducible, controllable and direct wet chemical synthesis method for ZnO:Co nanoparticles, which consists in the simultaneous addition of reactants (abbreviated as WCS-SimAdd) as acetate salts and oxalic acid, under pH control, in the presence of an anti-agglomeration agent. The intermediate compounds (hydroxy-oxalate type precursors), are precipitated and transformed into final products (zinc oxide nanoparticles), by a thermal decomposition process. In order to have a better understanding of the processes that take place during the thermal decomposition of the hydroxy-oxalate precursor, the thermal analysis was correlated with the evolved gas analysis (TG–DTA–FT-IR). To our knowledge, until now no investigation using TG–DTA–FT-IR was performed for the study of the decomposition processes of zinc hydroxy-oxalate precursor into zinc oxide nanoparticles. Structural, morphological and optical characterization was performed both for the precursors, and/or final products, with emphasis on the sample quality (i.e. homogeneity, substitution of Co for Zn sites), and sample reproductibility with controlled crystallite size and Co content. Thus, a double correlation between the synthesis conditions – structural, morphological characteristics and optical and magnetic properties – was established.

2. Experimental

The nanocrystalline $Zn_{1-x}Co_xO$ (x=0.05, 0.10, and 0.15) samples were prepared by the wet chemical synthesis route – simultaneous addition of reagents (WCS-SimAdd), using acetates as the corresponding starting salts and oxalic acid as precipitating reagent. Zinc acetate dihydrate, $Zn(CH_3COO)_2 \cdot 2H_2O$ (99.9%, Merck), cobalt acetate tetrahydrate, $Co(CH_3COO)_2 \cdot 4H_2O$ (99,9%, Merck) and oxalic acid dihydrate, $H_2C_2O_4 \cdot 2H_2O$ were used. Aqueous solutions of acetates (0.5 M) and oxalic acid (0.5 M) were prepared. The precipitation was carried out under continuous magnetic stirring and the pH value was adjusted to 8 ± 0.2, by adding ammonium hydroxide solution (NH_4OH). Due to the strong basic hydrolysis of the cobalt acetate, the ammonia volume required to adjust the pH considerably decreases for the sample prepared with 10 and 15 at% cobalt. Also, tetraethylammonium hydroxide, $(C_2H_5)_4N(OH)$ was used as an anti-agglomeration agent. The post-precipitation stages consisted in a 24 h aging, separation by filtering and drying. The thermal treatment of the precipitate was performed at 500 °C, for 2 h, in air with a heating rate of 300 °C/h.

The as-obtained and calcined precipitate were characterized by Fourier transform infrared spectroscopy (FTIR) (Jasco 610 FTIR Spectrometer, KBr pellets technique), X-ray diffraction XRD (Bruker AXS D8 Discover diffractometer, 40 kV, 40 mA, $\lambda_{CuK\alpha1}$=154,056 Å). Moreover, the precipitates were characterized by thermogravimetric TG and differential thermal analysis DTG (Mettler Toledo TGA/SDTA851) and by FT-IR spectroscopy coupled with TG evolved gas analysis (Thermo Scientific Nicolet 6700 FT-IR Spectrometer equipped with TGA module; HR Nicolet TGA Vapor phase library). The transmission electron microscopy bright field (TEM) and high resolution images (HRTEM) coupled with selected area electron diffraction (SAED) were obtained using a 300 Kv Tecnai G^2 F30 S-TWIN transmission electron microscope. The diffuse reflectance UV–vis spectra (DRS) of the investigated powders were recorded using a Jasco V-650 spectrophotometer having an integrating sphere attachment. The ferromagnetic resonance (FMR) measurements were carried out, in the temperature range of −163 °C to 27 °C, on a X-band Bruker E-500 ELEXSYS spectrometer equipped with a variable temperature accessory. The spectra processing was performed by Bruker Xepr software. The electronic paramagnetic resonance (EPR) spectra were recorded using equal quantities of samples.

3. Result and discussion

It is well known that the chemical mechanism plays an important role in studying and controlling the precipitation/coprecipitation process, by the WCS-SimAdd technique [44]. Formation of $Zn_{1-x}Co_xO$ oxalate during the precipitation/coprecipitation processes of metal acetates with oxalic acid is governed by the following chemical reaction:

$$(1-x)Zn(CH3COO)_2 + xCo(CH_3COO)_2 + + H_2C_2O_4 \rightarrow Zn_{1-x}Co_xC_2O_{4\downarrow} + + 2CH_3COOH$$

The amount of ammonia added in order to increase the pH induces the increase of OH^- ions concentration in solution. If the OH^- concentration is higher, these anions could be able to coordinate the metal ions. In this case, hydroxyl-oxalate precipitates will be obtained ($M(C_2O_4)_{1-a}(OH)_{2a}$). The following ionic reaction governs the formation of the intermediate oxalate precipitate:

$$M^{2+} + C_2O_4^{2-} + 2aNH_4^+ + 2aOH^- \leftrightarrow aM(OH)_2 + (1-a) MC_2O_4 + 2aNH_4^+ + aC_2O_4^{2-}$$

$$M^{2+} + C_2O_4^{2-} + 2aNH_4^+ + 2aOH^- \leftrightarrow M(C_2O_4)_{1-a}(OH)_{2a}\downarrow + 2aNH_4^+ + aC_2O_4^{2-}$$

$M = Zn$, Co; $0 \ll a \ll 1$

3.1. Thermal analysis

Considering that the critical step in the synthesis of zinc oxide by wet-chemical methods is thermal decomposition of the precipitate, thermogravimetric and differential thermal analyses (TG–DTA) were conducted to understand the thermal behavior of the hydroxy-oxalate or oxalate type species and the results are illustrated in Fig. 1.

The TG–DTA analyses have revealed that the decomposition of the precipitates takes place in three (when forming the species $Zn_{0.95}Co_{0.05}O$ and $Zn_{0.90}Co_{0.10}O$) or two successive stages (when forming $Zn_{0.85}Co_{0.15}O$). The first stage occurs in

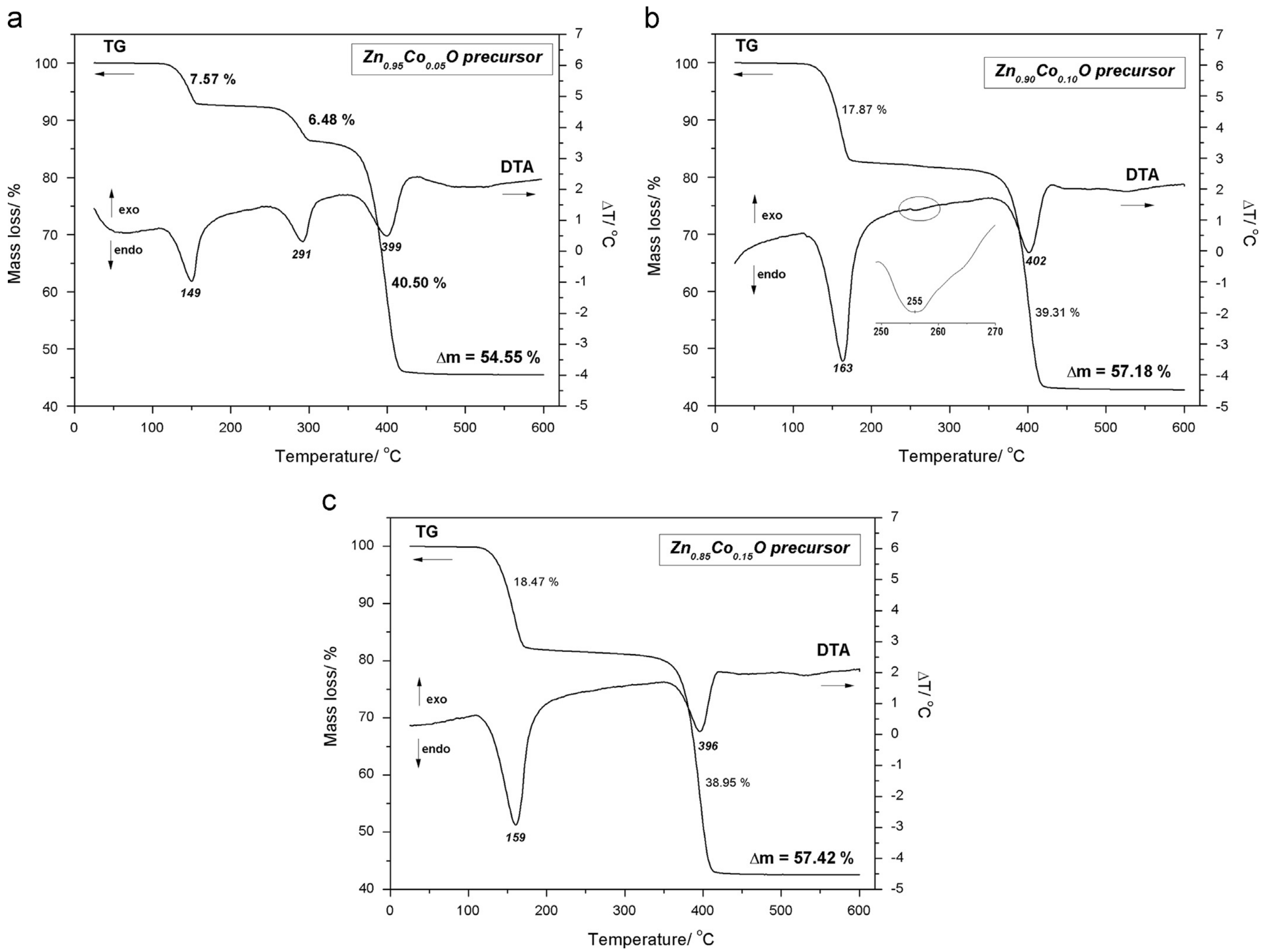

Fig. 1. TG and DTA curves for $Zn_{1-x}Co_xO$ precursors: (a) $x=0.05$; (b) $x=0.10$; (c) $x=0.15$.

the temperature range of 125–200 °C, with a mass loss of 7.5 wt% (corresponding to $Zn_{0.95}Co_{0.05}O$ formation), 17.8 wt% ($Zn_{0.90}Co_{0.10}O$) and 18.4 wt% ($Zn_{0.85}Co_{0.15}O$) and is attributed to the elimination of adsorbed water. A supplementary decomposition stage is observed for the precipitates prepared with 5% and 10 mol% Co, between 275 °C and 325 °C, corresponding to the decomposition of zinc hydroxide. The decomposition/transformation of this specie into zinc oxide is accompanied by a mass loss of 6.4 wt% for $Zn_{0.95}Co_{0.05}O$ sample. An insignificant mass loss followed by an endothermic effect can be observed at 266 °C for the $Zn_{0.90}Co_{0.10}O$ precipitate, indicating the presence of a small quantity of zinc hydroxide. The main decomposition step observed between 375 °C and 425 °C, with a significant mass loss of 40.5 wt% ($Zn_{0.95}Co_{0.05}O$), 39.3 wt% ($Zn_{0.90}Co_{0.10}O$) and 38.9 wt% ($Zn_{0.85}Co_{0.15}O$) is attributed to the decomposition of the oxalate group.

Taking into account these observations, it can be assumed that the decomposition of the precipitates takes place according to the following reactions:

$$125\text{–}200\ ^\circ\text{C}: Zn_{1-x}Co_xC_2O_4 \cdot aZn_{1-y}Co_y(OH)_2 \cdot bH_2O \rightarrow Zn_{1-x}Co_xC_2O_4 \cdot aZn_{1-y}Co_y(OH)_2 + bH_2O$$

$$275\text{–}325\ ^\circ\text{C}: Zn_{1-x}Co_xC_2O_4 \cdot aZn_{1-y}Co_y(OH)_2 \rightarrow Zn_{1-x}Co_xC_2O_4 + aZn_{1-y}Co_yO + aH_2O$$

$$375\text{–}425\ ^\circ\text{C}: Zn_{1-x}Co_xC_2O_4 \rightarrow Zn_{1-x}Co_xO + CO_2 + CO$$

No significant weight loss was observed for temperatures higher than 500 °C in the TG curves, indicating that the oxalate intermediates were completely decomposed.

3.2. TG–FTIR analysis

Information regarding the decomposition pattern of species generated during the decomposition of the hydroxi-oxalate or oxalate type precipitates was obtained from TG coupled with FTIR analysis. Fig. 2 presents the DTG curves associated with the total infrared absorbance profiles (Gram–Schmidt curve – a–c) of the evolved gases, as a function of time and the FT-IR profile of the gas evolved at different times/temperature (d–f). The two main decomposition stages are accompanied by a major gas release occurring between 125–200 °C and 375–425 °C. A supplementary gas release, between 275 °C and 325 °C, can be observed only for the $Zn_{0.95}Co_{0.05}O$ precipitate. It can be seen that the temperature of the IR

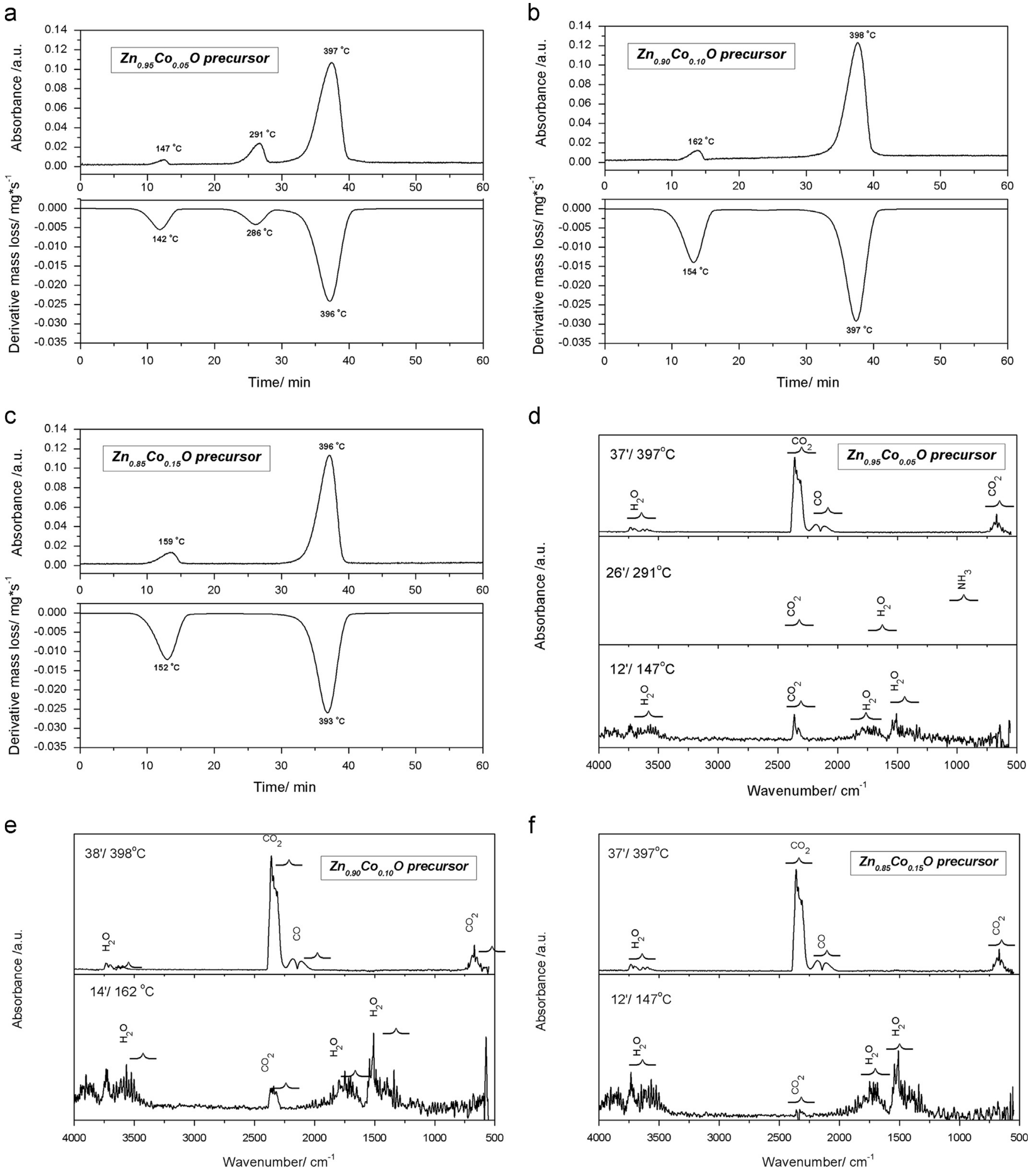

Fig. 2. Gram–Schmidt diagram coupled with DTG curve (a–c) and FT-IR spectra of the gases evolved during the thermal treatment of the precursors at different firing times (d–f).

absorbance peaks (Gram–Schmidt curve) is similar to that of the weight-loss maxima (DTG plot). The FT-IR characteristic absorbance bands of the main gaseous products – H_2O, CO_2, CO and NH_3 – evolved during the thermal treatment of the precipitates can be observed at different times: $\nu_{O–H}\sim 3400$–$4000\ cm^{-1}$, $\delta_{O–H}\sim 1300$–$1900\ cm^{-1}$ for H_2O; $\nu_{CO}\sim 2360\ cm^{-1}$ for CO_2; $\nu_{CO}\sim 2184$ and $2110\ cm^{-1}$ for CO; $\delta_{N–H}\sim 965$—$930\ cm^{-1}$ for NH_3 [45,46]. In the temperature range

125–200 °C, the released gases consist of H_2O adsorbed water and, CO_2, adsorbed from the atmosphere. The release of water in the temperature range 275–325 °C/26 min, for the $Zn_{0.95}Co_{0.05}O$ species is correlated with the decomposition of zinc hydroxide amorphous phase. Also, the presence of ammonia traces can be explained by the decomposition of small amounts of ammonium oxalate, formed during the precipitation or by the removal of the ammonia adsorbed on the surface of zinc hydroxide particles.

As the thermal treatment continues and the temperature increases, all the precipitates simultaneously release carbon dioxide and carbon monoxide (FT-IR spectra at minute 37–38, 397–398 °C) due to the decomposition of zinc oxalate. The water characteristic vibration bands are present, meaning that the dehydration was not completed and small quantities of water were trapped into the oxalate structure.

3.3. X-ray diffraction

The XRD patterns of the $Zn_{1-x}Co_xO$ and corresponding synthesized precipitate samples are presented in Fig. 3a and b. It is well known that, generally, the as-synthesized precipitates present an amorphous structure. The XRD patterns of the precipitate powders (Fig. 3a) exhibit typical diffraction peaks corresponding to the monoclinic structure of the zinc oxalate dihydrate, $ZnC_2O_4 \cdot 2H_2O$ (JCPDS card no. 01-0715157). In this context the presence of the zinc hydroxide phase observed by the thermal analysis for the $Zn_{0.95}Co_{0.05}O$ precursor could be explained by taking into consideration its amorphous structure character. In the 2θ: 5–15° range of the diffractogram, the shape indicates an amorphous component of the precipitates which increases with Co^{2+} cations concentration for the $Zn_{0.90}Co_{0.10}O$ and $Zn_{0.85}Co_{0.15}O$ species. Also, no diffraction peaks corresponding to cobalt oxalate or cobalt hydroxide based compounds were identified.

The XRD pattern of the prepared ZnO and $Zn_{1-x}Co_xO$ samples are presented in Fig. 3b. It is discovered that all samples possess a typical hexagonal wurtzite structure by comparison with the data from JCPDS standard file – PDF no. 36-1451, space group $P6_3mc$ (186). In the case of 5 mol% Co doping, no additional diffraction peaks were found, suggesting that the ZnO structure is not disturbed by the substitution, and there are no crystalline impurities in the sample. At low doping concentrations (above 5%), the Co ions can be incorporated into the ZnO crystal structure to form a solid solution. For the $Zn_{0.90}Co_{0.10}O$ sample, weak diffraction peaks belonging Co_3O_4 are detected. The strongest reflection peaks for Co_3O_4 are evidenced at higher cobalt concentration.

The calculated values for the crystallite size, lattice parameters a and c, and the crystal lattice distortion degree are shown in Table 1. Using the Scherrer formula, the average crystallite sizes calculated for the (101) and (100) peaks were about 42 nm for undoped ZnO. For the 5 mol% mol Co, the crystallite size has decreased to 30 nm, indicating that the presence of Co^{2+} ions inhibits the nucleation and the growth of the nanocrystals. For high cobalt concentration, an increase of the crystallite size can be observed, 35 nm for the 10 mol% Co, and 38 nm for the 15 mol% Co.

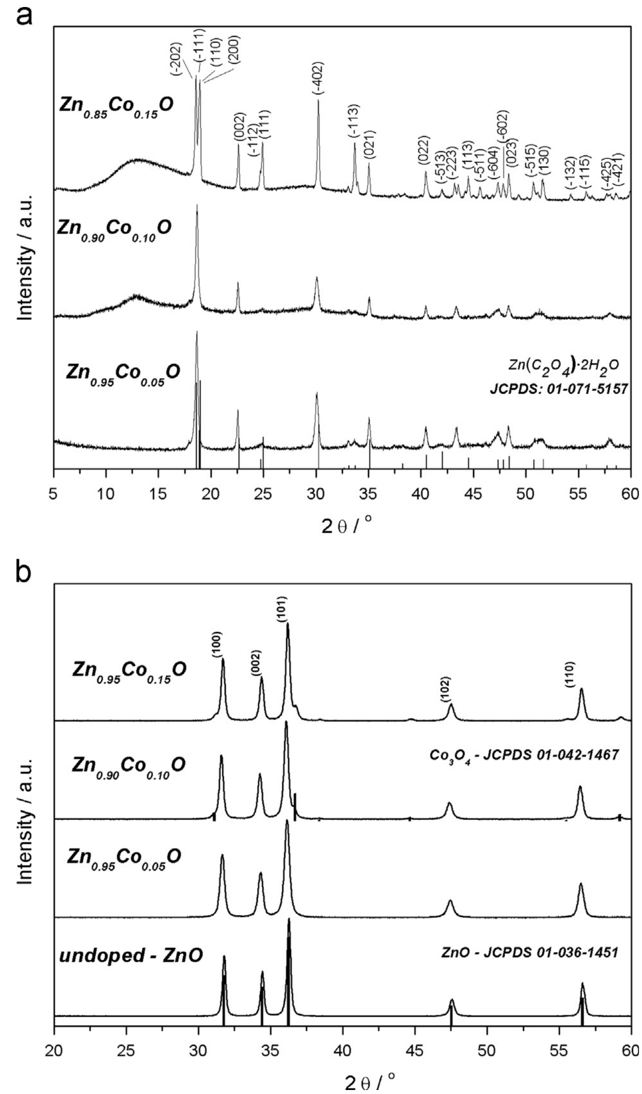

Fig. 3. (a) XRD patterns of the obtained $Zn_{1-x}Co_xO$ precursor powders – the diffraction peaks are indexed on the basis of the powder diffraction file JCPDS 01-071-5157; (b) diffraction pattern of undoped and Co doped ZnO nanoparticles.

The XRD patterns show that the ZnO lattice parameters slightly increase for the ZnO sample with a 5 wt% cobalt concentration. This increase is surprising since the ionic radius of cobalt (0.58 Å) is smaller than the ionic radius of zinc (0.60 Å) in the tetrahedral coordination. On the other hand, Djerdj et al. have suggested that an expansion of the structure is expected when Co^{2+} is incorporated into the ZnO structure in such a way that its coordination number is increased [19]. If the Co^{2+} ions are present in the octahedral coordination, its ionic radius increases to 0.65 Å for the low spin state, and to 0.74 Å in the high spin state. The octahedral coordination is possible only if Co^{2+} is incorporated into the structure at an interstitial site [19,20]. ZnO nanocrystals arise both from zinc hydroxide (291 °C) and zinc oxalate thermal decomposition (397 °C).

A direct consequence of the interstitial accommodation of Co^{2+} is the enhancement of the concentration of the lattice defects which can be correlated with the ZnO lattice distortion

Table 1
Crystallite sizes and unit cell parameters calculated according to the XRD data and the distortion degree calculated according to the lattice parameters.

Co concentration %	Crystallite size (nm)	Cell parameter *a* (Å)	Cell parameter *c* (Å)	Distortion degree
0	42	3249	5207	10,190
5	30	3251	5210	10,191
10	35	3250	5205	10,196
15	38	3251	5206	10,198

degree defined as the ratio $R==2a(2/3)^{1/2}/c$, where a, c are the calculated lattice parameters [28,29].

3.4. FT-IR spectroscopy

The infrared absorption (FT-IR) spectra recorded for the as-obtained precipitate samples (Fig. 4a) present the zinc oxalate characteristic absorption bands. The large band observed at approximately 3382 cm^{-1} can be attributed to the water – ν (O–H) stretching vibration, whereas the band at 2340 cm^{-1} is assigned to the adsorbed CO_2 gas. A low intensity band at approximately 3170 cm^{-1} corresponding to the ammonium – ν(N–H) stretching vibration, can be observed in all the precipitate spectra [47]. The asymmetric $\nu_{asym}(COO^-)$ and the symmetric $\nu_{sym}(COO^-)$ stretching modes observed at 1617 cm^{-1} and 1362, and 1320 cm^{-1}, respectively, are assigned to the oxalate modes [49,50]. The difference in their frequencies $\Delta\nu(COO^-)=\nu_{asym}(COO^-)-\nu_{sym}(COO^-)$ is around 255 cm^{-1} suggesting a bidentate coordination of the oxalate with Zn, in which four O atoms are involved [50]. Three low intensity bands at 816, 739 and 610 cm^{-1} are also observed in the spectra and are attributed to the δ(O–C═O) bridging oxalate group and to the coordination between metal ions with the carboxylates sites of the oxalate ion ν(O–Zn–O) and ν(Zn–O) [51]. The bands at 489 and 440 cm^{-1} are attributed to the interaction of the metal–oxygen vibration ν (Zn–O) [52].

The FT-IR spectra of undoped ZnO and doped ZnO:Co samples (Fig. 4b) confirm the total conversion of the precipitates into zinc oxide by thermal treatment. The strong Zn–O absorption bands at 440, 490 and 525 cm^{-1} suggest that the main phase of the as-prepared particles is zinc oxide. No evidence of the oxalate group characteristic vibrations is found in the FT-IR spectra of all samples.

The FT-IR spectrum of undoped ZnO (4000–400 cm^{-1}) is presented in the inset of the Fig. 4b. The low intensity bands at 3425, 1630 and 2350 cm^{-1} assigned to the O–H stretching, O–H bending and O═C═O stretching vibrations, respectively, are due to the atmospheric water and carbon dioxide adsorbed on the nanoparticles surface. Two characteristic absorption bands at 600 and 678 cm^{-1} attributed to Co–O stretching vibration for the Co_3O_4 phase are observed in the spectra of the high cobalt concentration sample [53]. As the XRD analyses has already illustrated, these bands cannot be identified in the $Zn_{0.95}Co_{0.15}O$ spectrum. But, in this case, an increase in the absorption band intensity at 489 cm^{-1} can be observed. That can be correlated with the Co–O stretching vibration observed at 507 cm^{-1}, for a CoO phase [53].

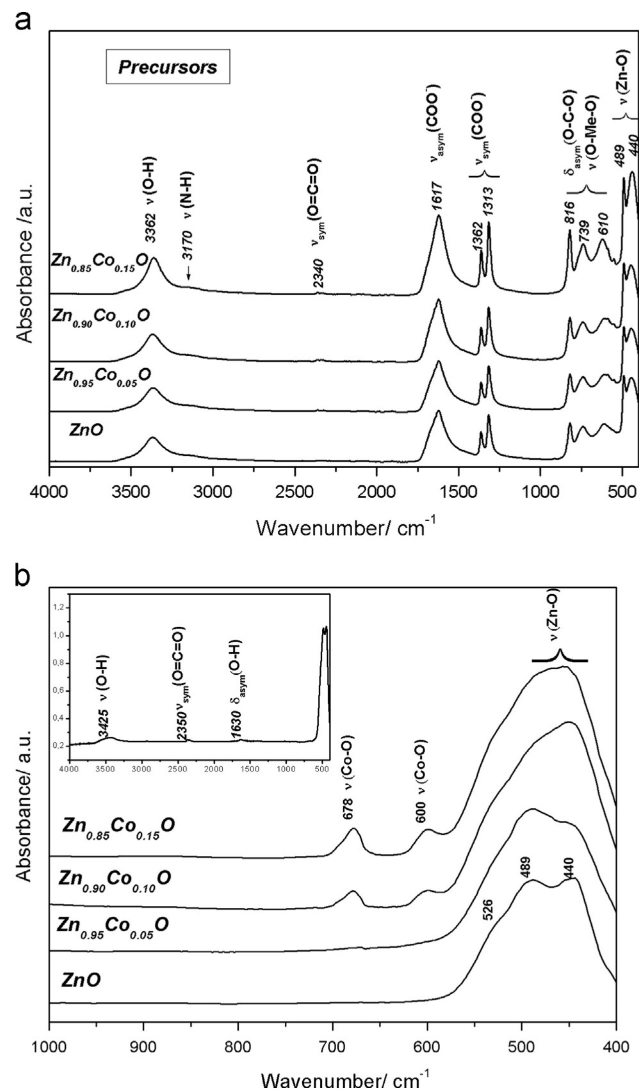

Fig. 4. (a) FT-IR spectra of ZnO and $Zn_{1-x}Co_xO$ precursors; (b) FT-IR spectra for undoped ZnO and Co doped ZnO samples (1000–400 cm^{-1}); inset – FT-IR spectra for undoped ZnO (4000–400 cm^{-1}).

3.5. TEM–HRTEM analysis

The TEM analysis (Fig. 5) obtained on the precursor powder provides a direct observation of the morphological and structural characteristics. The precipitate powder consists in nanocrystalline particles and aggregates, this behavior being

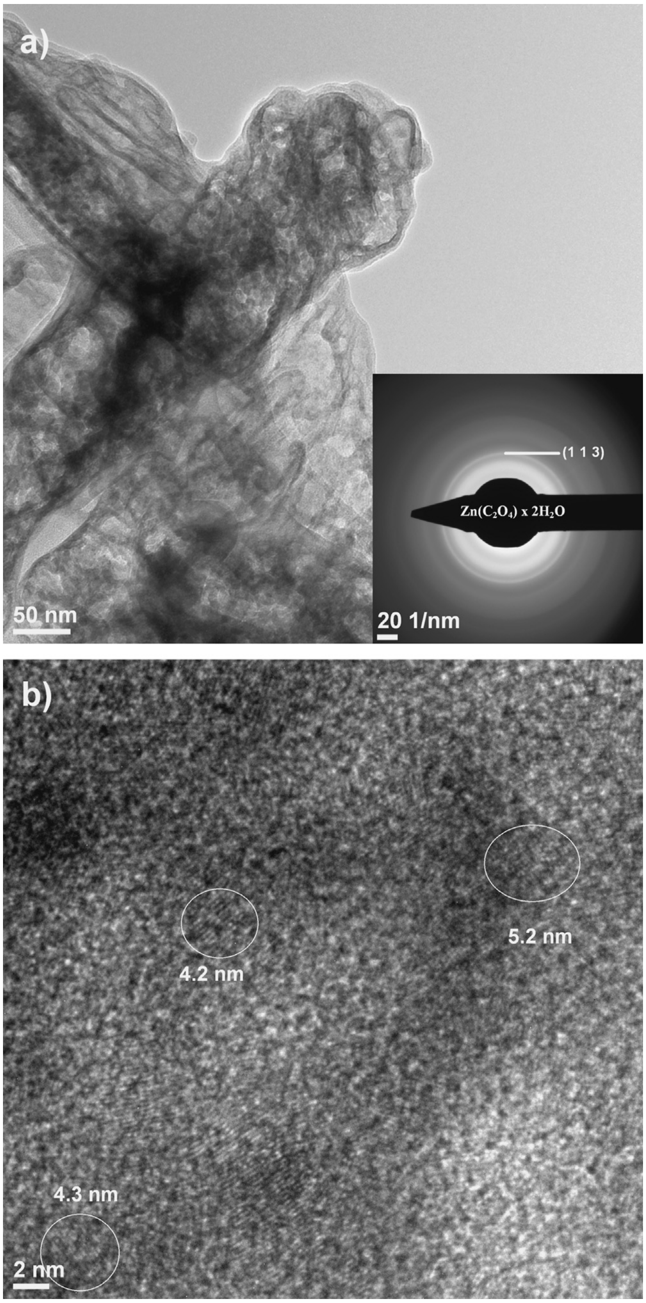

Fig. 5. TEM image and SAED pattern (inset) (a) and HRTEM pattern (b) of $Zn_{0.95}Co_{0.05}O$ precursor.

characteristic for the oxalate type precursors [32,43,51]. SAED (inset of Fig. 5a) and the high resolution pattern (Fig. 5b) illustrates the amorphous structure, but also the presence of very small crystallites (4–54–5 nm in size) of ZnC_2O_4.

The TEM bright field images of ZnO and Co doped ZnO samples (Fig. 6) illustrate the presence of the aggregates with different shape and lengths, formed by agglomerated spherical and polyhedral nanoparticles with sizes in the range of 28–38 nm. This tendency to form larger and denser nanoparticle aggregates during the thermal treatment is typical for zinc oxalate type precipitates [51]. The estimated crystallite sizes, according to the TEM analysis, confirm the calculated values from XRD. Thus, the $Zn_{0.95}Co_{0.05}O$ sample presents the lowest crystallite size, estimated at 28 nm, while an increase tendency of the crystallite size is observed with an increase of cobalt concentration. The granulometric distribution of the samples shows that the undoped zinc oxide has a monomodal distribution, while for all other samples, the grain size distribution is bimodal, and for the highest concentration of Co the grain size distribution is almost trimodal.

From the SAED patterns presented in insets of Fig. 6 a, c–e, and g, we can see distinguishable diffraction patterns corresponding to the hexagonal structure of zinc oxide while for the 15% Co doped ZnO a (111) orientation of the lattices appears corresponding to the Co_3O_4, also being in agreement with the X-Ray diffraction data. A closer view into the crystal structure of ZnO nanoparticles is achieved by HRTEM images shown in Fig. 7. All the HRTEM images are presenting nanoparticles with a good crystallinity with a clear resolution of lattice fringes of $d = 1.91$ Å, 2.48 Å, 2.6 Å and 2.82 Å corresponding to the crystallographic planes (102), (101), (002) and (100) corresponding to hexagonal ZnO (Fig. 8).

3.6. Optical characterization

The substitution of Zn sites for Co into the ZnO structure was verified by conventional UV–vis spectroscopy. Fig. 9a presents the optical absorption spectra of the $Zn_{1-x}Co_xO$ series using as a reference the undoped ZnO spectrum. The insertion of the Co ions into the ZnO structure leads to the appearance of three additional absorption bands at about 568, 613 and 654 nm. They are frequently observed in Co doped ZnO samples and were attributed to 4A2(F)→2E(G), 4A2(F)→2T1(P) and 4A2(F)→2A1(G) transitions, indicating that the Co^{2+} ions substitute the Zn^{2+} ions in ZnO and that their valence is 2+ [54,55]. These bands are assigned to the typical *d–d* transitions of Co^{2+} ions with $3d^7$ high-spin configuration, involving crystal field levels of Co^{2+} in the tetrahedral coordination [56,57]. Based on the absorption spectra, the direct band-gap of all samples is calculated from the following relationship:

$$(\alpha E) = A(E - E_g)^{n/2}$$

where α – optical absorption coefficient, $\alpha = A/d'$; A – is the measured absorbance and d' – the thickness of sample in a UV–vis cell (0.4 cm), E – the photon energy, E_g – the direct band gap of the sample. The extrapolation of the linear part of the curve of $(\alpha E)^2$ vs. E to the $\alpha E=0$ (where $E=E_g$) allows the calculation of the direct band-gap for all samples. The band gap of pure ZnO is about 3.2 eV, in agreement with the literature data [56,58–60]. The sharp absorption peak of the undoped ZnO changes into a broad peak shifted to higher wavelengths when the concentration of Co ions in ZnO increases. As can be observed in Fig. 9b, the band gaps decreases form 3.2 eV in undoped ZnO to 2 eV when the Co^{2+} concentration reached 15%. This redshift of the band gap edge by the incorporation of Co into ZnO was reported before [61] and was associated with *sp–d* exchange interactions between the band electrons and the localized *d* electrons of the Co^{2+} ions substituting Zn ions. Seemingly,

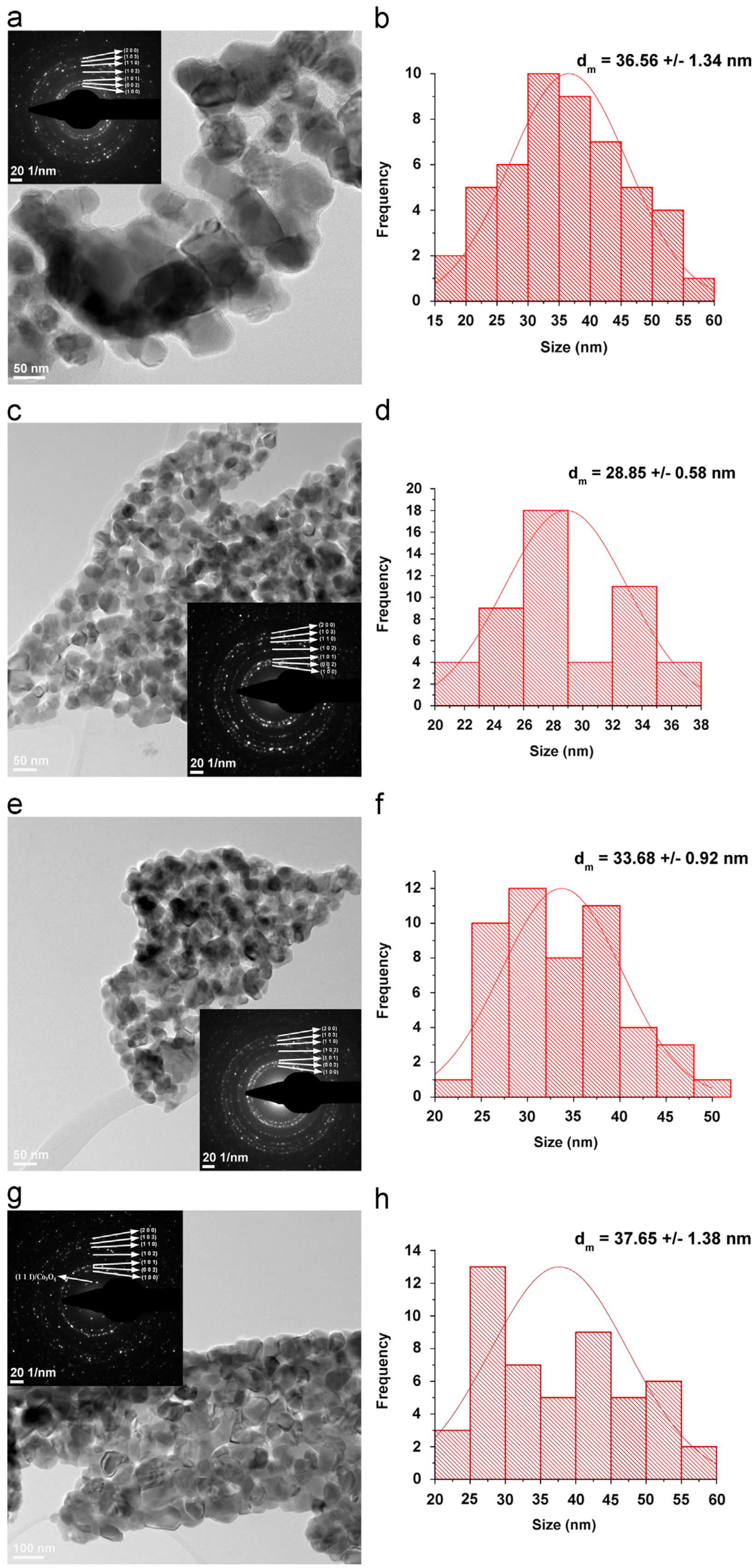

Fig. 6. TEM images of ZnO (a), $Zn_{0.95}Co_{0.05}O$ (c), $Zn_{0.90}Co_{0.10}O$ – e, $Zn_{0.85}Co_{0.15}O$ (g) samples. The corresponding SAED patterns are presented in the inset for each sample and grain size distribution histograms for ZnO (b), $Zn_{0.95}Co_{0.05}O$ (d), $Zn_{0.90}Co_{0.10}O$ (f), $Zn_{0.85}Co_{0.15}O$ (h) samples.

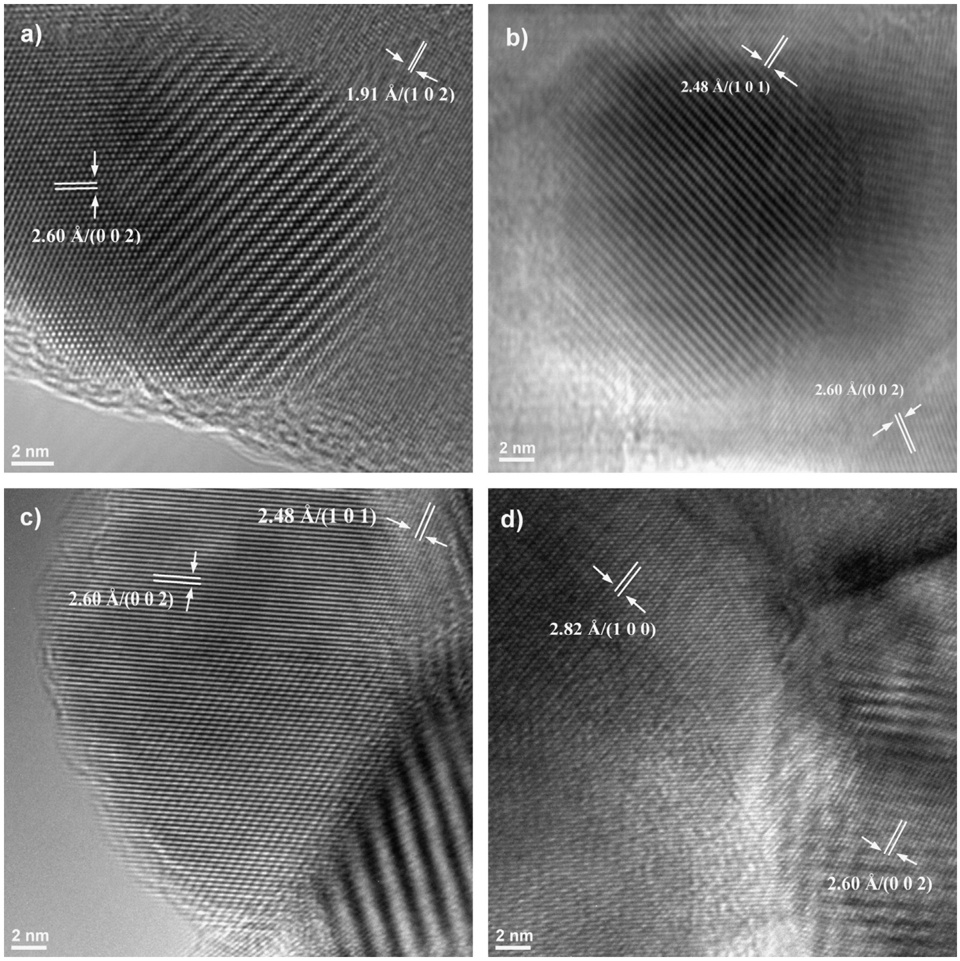

Fig. 7. HRTEM images of ZnO (a), $Zn_{0.95}Co_{0.05}O$ (b), $Zn_{0.90}Co_{0.10}O$ (c), $Zn_{0.85}Co_{0.15}O$ (d) samples.

the incorporation of Co^{2+} into ZnO in substitution positions occurs even at higher concentrations of dopant. However, the presence of Co_3O_4 in $Zn_{1-x}Co_xO$ ($x \geq 0.05$) (confirmed by XRD measurements) could be also responsible for the redshift of the band gap. Co_3O_4 is known as a black powder, having strong absorption in the whole UV–vis range. Thus, its presence also increases the absorption of $Zn_{1-x}Co_xO$ ($x \geq 0.05$) in the UV–vis region of the spectrum [29].

3.7. EPR spectroscopy

The EPR spectroscopy was performed in order to understand how the Co ions are incorporated in the ZnO lattice and to investigate the magnetic behavior of the samples. In this type of compounds, the cobalt atoms substitute the zinc atoms and the neutral charge state is Co^{2+} (a $3d^7$ configuration). Co^{59} has $I=7/2$ which gives rise in single crystals to an eight line hyperfine pattern. The EPR spectra of $Zn_{1-x}Co_xO$ measured at -163 °C are presented in Fig. 9. For the $Zn_{0.95}Co_{0.05}O$ and $Zn_{0.90}Co_{0.10}O$ samples, the spectra are composed of an intense line near 1500 G and a small line near 3000 G. These line correspond to the effective $g_{zz}=4.4$, $g_{xx}=2.27$, respectively suggesting that the system symmetry is axially distorted.

The absence of the hyperfine structure could be due to an increasing number of randomly distributed defects, which enhances disorder of the crystalline field at Co^{2+} sites [62]. Usually the isolated Co^{2+} ions give a sharper line at 1500 G [63,64]. In our case of the sample signal is broad, the line width being about 300 G. This behavior is due to the large concentration of spins which is known to contribute to the signal broadening. A similar broadening behavior was observed in a ZnO thin epitaxial film doped with 10% Co [65].

The EPR spectra of the sample doped with $x=0.15$ shows in addition of the line at 1500 G another intense line at 2800 G whose origin will be explained later. As it can be seen in Fig. 10, the EPR spectra of the Co dopant in the ZnO nanopowders depend strongly on the Co concentration. By increasing the Co concentration the line intensity decreases. The double integration of the EPR line can be used to estimate the relative signal corresponding to each sample. The evaluated integral intensity of the spectrum, IEPR, resulted by a double integration of the EPR experimental spectra is proportional to the spin concentration [66]. Fig. 10 shows the Co concentration dependence of the integral intensity corresponding to the most intense line.

It can be noticed that by increasing the Co concentration up to a value of 10%, the intensity decreases abruptly and then

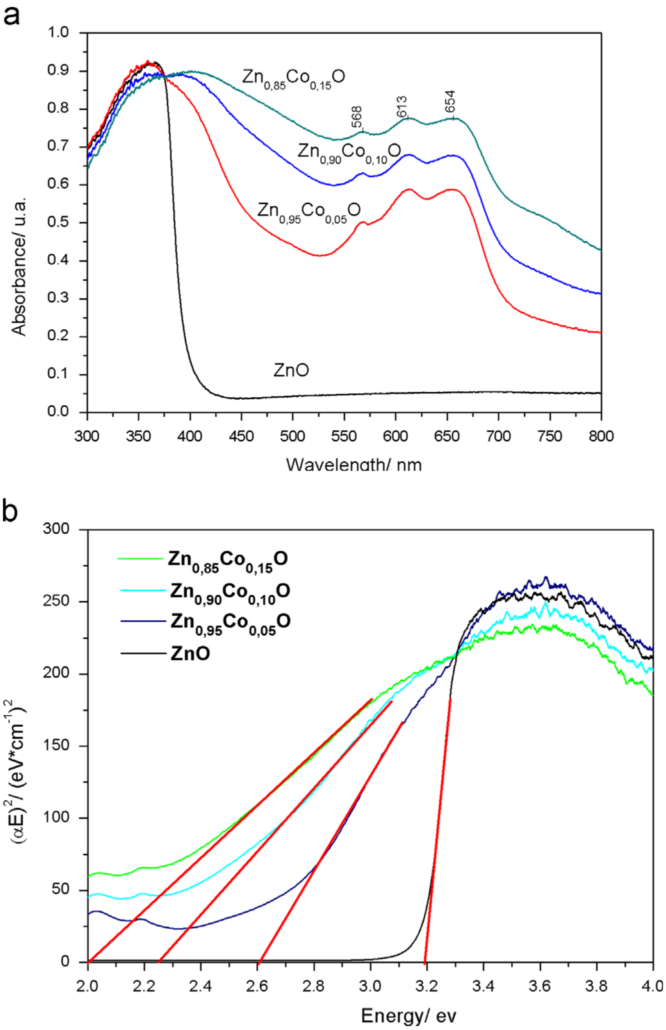

Fig. 8. UV–vis absorption spectra (a) and evolution of $(\alpha E)^2$ vs. E curves (b) corresponding to ZnO and $Zn_{1-x}Co_xO$ samples.

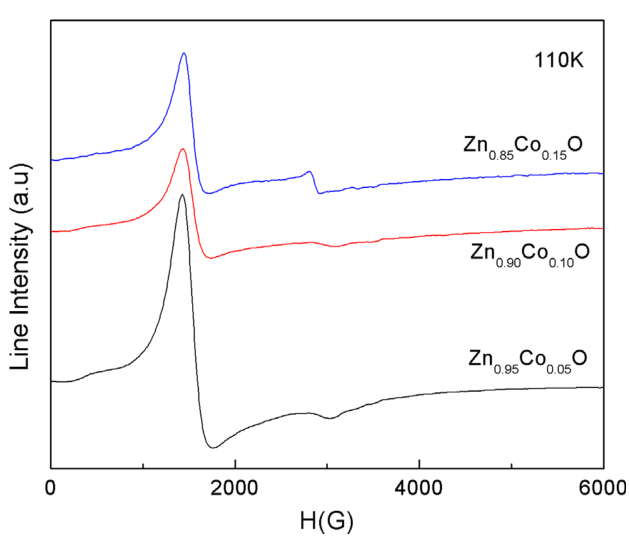

Fig. 9. EPR spectra of $Zn_{1-x}Co_xO$ with $x=0.05$, $x=0.1$ and $x=0.15$, respectively measured at 110 K.

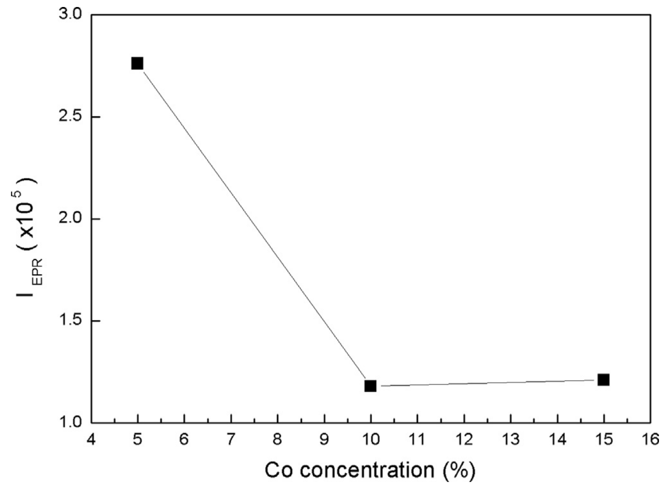

Fig. 10. The variation of the EPR integral intensity with the Co concentration for the signal appeared at 1500 G.

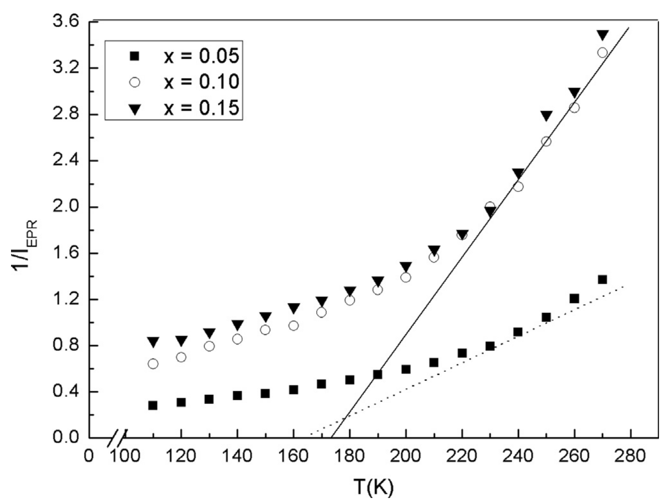

Fig. 11. The temperature dependence of 1/IEPR for $Zn_{1-x}Co_xO$ with $x=0.05$, $x=0.10$ and $x=0.15$.

remains approximately constant. Therefore, an increase of the concentration up to 10% leads to a decrease in spin concentration. This shows that for Co concentration higher than 10%, besides Co^{2+} ions, responsible for EPR signal, appear Co ions with a different oxidation state. This conclusion is sustained by the presence of the secondary phase of Co_3O_4 in the sample with concentration higher than 10%. The presence of Co_3O_4 was evidence by XRD measurements. Previous studies have shown that Co_3O_4 is an antiferromagnetic compound whose EPR signal is composed of a wide line located at a resonance field of about 2800 G [67]. The sample $Zn_{0.85}Co_{0.15}O$ presents a small EPR line at 2800 G and this line probably could be attributed to the Co_3O_4. Direct information about the magnetic state of the $Zn_{1-x}Co_xO$ powders can be obtained from the variation of the EPR spectrum integral intensity, IEPR, with the temperature [65]. The intensity IEPR (T) is proportional to the spin susceptibility of the paramagnetic species taking part in resonance. We choose to integrate the most intense line of the spectra, the one with the resonance field at 1500 G.

In Fig. 11 we show the temperature dependence of 1/IEPR for $Zn_{1-x}Co_xO$ with $x=0.05$, $x=0.10$ and $x=0.15$. IEPR (T) was obtained by the double integration of the corresponding EPR spectra. In the high temperature limit, the variation of IEPR (T) can be described by:

$$I_{\mathrm{EPR}}\ (T) \sim \frac{C(x)}{T-\theta(x)}$$

where C is the Curie constant and θ the Curie–Weiss temperature, both being dependent on the dopant concentration, x.

The numerical value of θ is obtained from the linear extrapolation of the high temperature part of 1/IEPR, as indicated by the straight line in Fig. 11. The evaluated θ values are -113 °C, -98 °C, and -93 °C for the samples with $x=0.05$, $x=0.10$ and $x=0.15$, respectively. The positive sign of the Curie–Weiss temperatures indicates that a ferromagnetic coupling between the Co^{2+} ions is present in our samples.

4. Conclusions

Co doped ZnO nanoparticles have been synthesized by a wet-chemical synthesis route using the SimAdd technique. The full understanding of decomposition mechanism of the as-obtained oxalate precipitate was achieved by FTIR, DTA–TG and TG–DTA–FT-IR analyses. The crystallinity, as well as the morphology of Co doped ZnO nanoparticles are considerably affected by the Co concentration. The XRD studies reveal a hexagonal wurtzite-type structure for all the $Zn_{1-x}Co_xO$ samples. TEM investigations show an average particle size range from 28 to 37 nm and a polyhedral and spherical morphology with a tendency to form aggregates. The formation of a Co_3O_4 secondary phase was evidenced by XRD, FTIR, UV–vis and EPR investigations. From the analysis of temperature dependence of the EPR integral intensity, the Curie–Weiss temperatures were evaluated and a ferromagnetic behavior was revealed for the investigated samples. On the other hand, the paper evidences the possibility to modulate the Co-doped ZnO morphological characteristics and, the optical and magnetic properties by this wet-chemical method.

Acknowledgments

This work was supported by CNCSIS-UEFISCSU, project number PNII-IDEI no. 4/2010, code ID-106 and POS CCE ID 574 and code SMIS CSNR 12467.

References

[1] D.C. Look, D.C. Reynolds, J.R. Sizelove, R.L. Jones, C.W. Litton, G. Cantwell, W.C. Harsch, Electrical properties of bulk ZnO, Solid State Commun. 105 (6) (1998) 399–401.

[2] D.C. Look, Recent advances in ZnO materials and devices, Mater. Sci. Eng. B 80 (2001) 383–387.

[3] Ü. Özgür, Y. Alivov, A. Teke, A. Reshchikov, S. Doğan, V. Avrutin, S.-J. Cho, H. Morkoç, A comprehensive review of ZnO materials and devices, J. Appl. Phys. 98 (2005) 041301.

[4] S.B. Ogale, Thin Films and Heterostructures for Oxide Electronics, Springer, New York, 2005.

[5] N.H. Nickel, E. Terukov, Zinc Oxide – A Material for Micro and Optoelectronic Applications, Springer, Netherlands, 2005.

[6] C. Jagadish, S.J. Pearton, Zinc Oxide Bulk, Thin Films, and Nanostructures, Elsevier, New York, 2006.

[7] A. Janotti, C. Van de Walle, Fundamentals of zinc oxide as a semiconductor, Rep. Prog. Phys. 72 (2009) 126501.

[8] D.G. Thomas, The exciton spectrum of zinc oxide, J. Phys. Chem. Solids 15 (1960) 86–96.

[9] A. Mang, K. Reimann, St. Rübenacke, Band gaps, crystal-field splitting, spin–orbit coupling, and exciton binding energies in ZnO under hydrostatic pressure, Solid State Commun. 94 (4) (1995) 251–254.

[10] D.C. Reynolds, D.C. Look, B. Jogai, Optically pumped ultraviolet lasing from ZnO, Solid State Commun. 99 (12) (1996) 873–875.

[11] D.M. Bagnall, Y.F. Chen, Z. Zhu, T Yao, S. Koyama, M.Y. Shen, T. Goto, Optically pumped lasing of ZnO at room temperature, Appl. Phys. Lett. 70 (1997) 2230.

[12] V. Srikant, D.R. Clarke, On the optical band gap of zinc oxide, J. Appl. Phys. 83 (1998) 5447.

[13] D.C. Reynolds, D.C. Look, B. Jogai, Valence-band ordering in ZnO, Phys. Rev. B 60 (1999) 2340–2344.

[14] P.S. Reddy, G.R. Chetty, S. Uthanna, B.S. Naidu, P.J. Reddy, Optical properties of spray deposited ZnO films, Solid State Commun. 77 (12) (1991) 899–901.

[15] K. Keis, E. Magnusson, H. Lindström, S.E. Lindquist, A. Hagfeldt, A 5% efficient photoelectrochemical solar cell based on nanostructured ZnO electrodes, Sol. Energy Mater. Sol. Cells 73 (2002) 51–58.

[16] B. Yukas, P. Yang, Nanowire-based all oxide solar cells, J. Am. Chem. Soc. 131 (2009) 3756–3761.

[17] C.Y. Hsu, T.F. Ko, Y.M. Huang, Influence of ZnO buffer layer on AZO film properties by radio frequency magnetron sputtering, J. Eur. Ceram. Soc. 28 (2008) 3065–3070.

[18] Y.F. Hsu, Y.Y. Xi, A.B. Djurišić, W.K. Chan, ZnO nanorods for solar cells: hydrothermal growth versus vapour deposition, Appl. Phys. Lett. 92 (2008) 133507–133509.

[19] I. Djerdj, G. Garnweitner, D. Arčon, M. Pregelj, Z. Jagličić, M. Niederberger, Diluted magnetic semiconductors: Mn/Co-doped ZnO nanorods as case study, J. Mater. Chem., 18, , 2008, p. 5208–5217.

[20] J. Hays, K.M. Reddy, N. Graces, M. Engelhard, V. Shuttanandan, M. Luo, C. Xu, N.C. Giles, C. Wang, S. Thevuthasan, A. Punnoose, Effect of Co doping on the structural, optical and magnetic properties of ZnO nanoparticles, J. Phys.: Condens. Matter 19 (2007) 266203.

[21] J. Volk, T. Nagata, R. Erdelyi, I. Barsoni, A.L. Toth, I.E. Lukacs, Z. Czigany, H. Tomimoto, Y. Shingaya, T. Chikyow, Highly uniform epitaxial ZnO nanorod arrays for nanopiezotronics, Nanoscale Res. Lett. 4 (2009) 699–704.

[22] T.S. Van den Heever, U. Büttner, W.J. Perold, A novel method to measure the generated voltage of a ZnO nanogenerator, Nanotechnology 22 (2011) 395204.

[23] A. Becheri, M. Dürr, L.P. Nostro, P. Baglioni, Synthesis and characterisation of zinc oxide nanoparticles: application to textiles as UV-absorbers, J. Nanopart. Res. 10 (2008) 679–689.

[24] A.J. Gimenez, J.M. Yanez-Limon, J.M. Seminario, ZnO-paper based photoconductive UV sensor, J. Phys. Chem. 115 (2011) 282–287.

[25] D.S. Bohle, C.J. Spina, Controlled Co(II) doping of zinc oxide nanocrystals, J. Phys. Chem. C 114 (2010) 18139–18145.

[26] X.M. Zhang, M.Y. Lu, Y. Zhang, L.J. Chen, Z.L. Wang, Fabrication of a high-brightness blue-light-emitting diode using a ZnO-nanowire array grown on GaN thin film, Adv. Mater. 21 (2009) 2767–2770.

[27] M. Willander, O. Nur, Q.X. Zhao, L.L. Yang, M. Lorenz, B.Q. Cao, J.Z. Pérez, C. Czekalla, G. Zimmermann, M. Grundmann, A. Bakin, A. Behrends, M. Al-Suleiman, A. El-Shaer, A. Che Mofor, B. Postels, A. Waag, N. Boukos, A. Travlos, H.S. Kwack, J. Guinard, D. Le Si Dang, Zinc oxide nanorod based photonic devices: recent progress in growth, light emitting diodes and lasers, Nanotechnology 20 (2009) 332001.

[28] M. Gaudon, O. Toulemonde, A. Demourgues, Green coloration of Co-doped ZnO explained from structural refinement and bond considerations, Inorg. Chem. 46 (2007) 10996–11002.

[29] M. Li, J. Xu, X. Chem, X. Zhang, Y. Wu, P. Li, X. Niu, C. Luo, L. Li, Structural and optical properties of cobalt doped ZnO nanocrystals, Superlattices Microstruct. 52 (2012) 824–833.

[30] T.M. Hammad, J.K. Salem, R. Harrison, The influence of annealing temperature on the structure, morphologies and optical properties of ZnO nanoparticles, Superlattices Microstruct. 47 (2010) 335–340.

[31] N. Hasuike, R. Deguchi, H. Katoh, K. Kisoda, K. Nishio, T. Isshiki, H. Harima, Structural properties of nanometre-sized ZnO crystal doped with Co, J. Phys.: Condens. Matter 19 (2007) 365223–365230.

[32] C.J. Raj, R.K. Joshi, B.R. Varma, Synthesis from zinc oxalate, growth mechanism and optical properties of ZnO nano/micro structures, Cryst. Res. Technol. 46 (2011) 1181–1188.

[33] J. Yang, X. Liu, L. Yang, Y. Wang, Y. Zhang, J. Lang, Effect of annealing temperature on the structure and optical properties of ZnO nanoparticles, J. Alloys Compd. 477 (2009) 632–635.

[34] G. Ambrožič, S.D. Škapin, M. Žigon, Z.C. Orel, The synthesis of zinc oxide nanoparticles from zinc acetylacetonate hydrate and 1-butanol or isobutanol, J. Colloids Interface Sci. 346 (2010) 317–323.

[35] N. Kiomarsipour, R.S. Razavi, Hydrothermal synthesis and optical property of scale- and spindle-like ZnO, Ceram. Int. 39 (2013) 813–818.

[36] J.C. Lin, C.P. Lee, K.C. Ho, Zinc oxide synthesis via a microemulsion technique: morphology control with application to dye-sensitized solar cells, J. Mater. Chem. 22 (2012) 1270–1273.

[37] P. Dolcet, M. Casarin, C. Maccato, L. Bovo, G. Ischia, S. Gialanella, F. Mancin, E. Tondello, S. Gross, Miniemulsions as chemical nanoreactors for the room temperature synthesis of inorganic crystalline nanostructures: ZnO colloids, J. Mater. Chem. 22 (2012) 1620–1626.

[38] O.R. Vasile, E. Andronescu, C. Ghitulica, B.S. Vasile, O. Oprea, E. Vasile, R. Trusca, Synthesis and characterization of nanostructured zinc oxide particles synthesized by pyrosol method, J. Nanopart. Res. 14 (2012) 1269.

[39] E. Dinu, E. Siebert, E. Andronescu, E. Djurado, L. Dessemond, C. Ghitulica, Nanocrystallites obtained through the pyrosol method, Phys. Status Solidi A 205 (2008) 1488–1493.

[40] S. He, M. Zheng, L. Yao, X. Yuan, M. Li, L. Ma, W. Shen, Preparation and properties of ZnO nanostructures by electrochemical anodization method, Appl. Surf. Sci. 256 (2010) 2557–2562.

[41] L. Ding, L. Zhang, L. Fan, Electrochemical route to the synthesis of ZnO microstructures: its nestlike structure and holding of Ag particles, Nano Res. Lett. 8 (2013) 78.

[42] D. Toloman, A. Mesaros, A. Popa, O. Raita, T.D. Silipas, B.S. Vasile, O. Pana, L.M. Giurgiu, Evidence by EPR of ferromagnetic phase in Mn-doped ZnO nanoparticles annealed at different temperatures, J. Alloys Compd. 551 (2013) 502–507.

[43] S. Suwanboon, P. Amornpitoksuk, A. Sukolrat, Dependence of optical properties on doping metal, crystallite size and defect concentration of M-doped ZnO nanopowders (M = Al, Mg, Ti), Ceram. Int. 37 (2011) 1359–1365.

[44] E.J. Popovici, L. Muresan, A. Hristea, E. Indrea, M. Vasilescu, Synthesis and characterization of europium activated yttrium oxide fine powders, J. Alloys Compd. 434–435 (2007) 809–812.

[45] L. Muresan, E.J. Popovici, E. Bica, A.I. Cadis, I. Perhaita, L.B. Tudoran, Investigation of thermal decomposition of yttrium–aluminium-based precursors for YAG phosphors, J. Therm. Anal. Calorim. 110 (2012) 341–348.

[46] A. Saponar, E.J. Popovici, I. Perhaita, G. Nemes, A.I. Cadis, Thermal behaviour of some ester derivates of p-tert-butyl calyx[n]arene, Therm. Anal. Calorim. 110 (2012) 349–356.

[47] B.B.V. Sailaja, T. Kebede, G.S. Raju, M.S.P. Rao, Thermal decomposition of ammonium dioxodiaquaperoxyoxalatouranate (VI) hydrate, Therm. Anal. Calorim. 386 (2002) 51–57.

[49] M.A. Gabal, A.A. El-Bellihi, H.H. El-Bahnasaw, Non-isothermal decomposition of zinc oxalate–iron(II) oxalate mixture, Mater. Chem. Phys. 81 (2003) 174–182.

[50] K. Nakamoto, Infrared and Raman Spectra of Inorganic and Coordination Compounds, John Wiley and Sons, New York, 1997.

[51] K. Elen, A. Kelchtermans, H. Van den Rul, R. Peeters, J. Mullens, A. Hardy, M.K. Van Bael, Comparison of two novel solution-based routes for the synthesis of equiaxed ZnO nanoparticles, J. Nanomater. 2011 (2011) (Article ID: 390621), http://dx.doi.org/10.1155/2011/390621.

[52] I. Luisetto, F. Pepe, E. Bemporad, Preparation and characterization of nano cobalt oxide, J. Nanopart. Res. 10 (2008) 59–67.

[53] C.W. Tang, C.B. Wang, S.H. Chien, Characterization of cobalt oxides studied by FT-IR, Raman, TPR and TG-MS, Thermochim. Acta 473 (2008) 68–73.

[54] C.J. Cong, J.H. Hong, K.L. Zhang, Effect of atmosphere on the magnetic properties of the Co-doped ZnO magnetic semiconductors, Mater. Chem. Phys 113 (2009) 435–440.

[55] L. El Mir, Z. Ben Ayadi, H. Rahmouni, J. El Ghoul, K. Djessas, H.J. von Bardeleben, Elaboration and characterization of Co doped, conductive ZnO thin films deposited by radio-frequency magnetron sputtering at room temperature, Thin Solid Films 517 (2009) 6007–6011.

[56] S. Colis, H. Bieber, S.B. Colin, G. Schmerber, C. Leuvrey, A. Dinia, Magnetic properties of Co-doped ZnO diluted magnetic semiconductors prepared by low-temperature mechanosynthesis, Chem. Phys. Lett. 422 (2006) 529–533.

[57] Y. Belghazi, D. Stoeffler, S. Colis, G. Schmerber, C. Ulhaq-Bouillet, J.L. Rehspringer, A. Berrada, H. Aubriet, J. Petersen, C. Becker, D. Ruch, A. Dinia, Magnetic properties of Al-doped $Zn_{0.95}Co_{0.05}O$ films: experiment and theory, J. Appl. Phys. 105 (2009) 113904.

[58] M. Bouloudenine, N. Viart, S. Colis, A. Dinia, Bulk $Zn_{1-x}Co_xO$ magnetic semiconductors prepared by hydrothermal technique, Chem. Phys. Lett. 397 (2005) 73–76.

[59] M. Bouloudenine, N. Viart, S. Colis, A. Dinia, $Zn_{1-x}Co_xO$ diluted magnetic semiconductors synthesized under hydrothermal conditions, Catal. Today 113 (2006) 240–244.

[60] J.H. Kim, H. Kim, D. Kim, Y.E. Ihm, W.K. Choo, Magnetic properties of epitaxially grown semiconducting $Zn_{1-x}Co_xO$ thin films by pulsed laser deposition, J. Appl. Phys. 92 (2002) 6066.

[61] S. Maensiri, J. Screesongmuang, C. Thomas, J. Klinkaewnarong, Magnetic behavior of nanocrystalline powders of Co-doped ZnO diluted magnetic semiconductors synthesized by polymerizable precursor method, J. Magn. Magn. Mater. 301 (2006) 422–432.

[62] S.K. Misra, S.I. Andronenko, K.M. Reddy, J. Hays, A. Punnoose, Magnetic resonance studied of Co^{2+}, J. Appl. Phys. 99 (08) (2006) M106.

[63] B.M. Weckhuysen, A. Verberckmoes, An, M.G. Uytterhoeven, F.E. Mabbs, D. Collison, E. de Boer, R.A. Schoonheydt, Electron spin resonance of high-spin cobalt in microporous crystalline cobalt containing aluminophosphates, J. Phys. Chem. B 104 (2000) 37–42.

[64] O. Raita, A. Popa, D. Toloman, M. Stan, A. Darabont, L.M. Giurgiu, Co^{2+} ions in ZnO powders as seen by magnetic resonance, Appl. Mag. Res. 40 (2) (2011) 245–250.

[65] N. Jedrecy, H.J. von Bardeleben, Y. Zheng, J.L. Cantin, Electron paramagnetic resonance study of $Zn_{1-x}Co_xO$: a predicted high-temperature ferromagnetic semiconductor, Phys. Rev. B 69 (2004) 041308.

[66] A.B. Mahmoud, H.J. von Bardeleben, J.L. Cantin, E. Chikoidze, A. Mauger, J. Appl. Phys. 101 (2007) 013902.

[67] N. Guskos, J. Typek, M. Maryniak, G. Zołnierkiewicz, M. Podsiadły, W. Arabczyk, Z. Lendzion-Bieluń, U. Narkiewicz, Effect of calcination and structural additives on the EPR spectra of nanocrystalline cobalt oxides, Mater. Sci.—Pol. 24 (4) (2006) 1095–1102.